

# The algorithm of microphysical parameter profiles of aerosol and small cloud droplets based on the dual wavelength Lidar data

Huige Di, Xinhong Wang, Ning Chen, Jing Guo, Wenhui Xin, Shichun Li, Yan Guo, Qing Yan, Yufeng Wang, Dengxin Hua\*

School of Mechanical and Precision Instrument Engineering, Xi'an University of Technology, Xi'an 710048, China

*Correspondence to:* Dengxin Hua (dengxinhua@xaut.edu.cn)

**Abstract.** This study proposed an inversion method of atmosphere aerosol or cloud microphysical parameters based on dual wavelength lidar data. The matching characteristics between aerosol/cloud particle size distribution and Gamma distribution were studied using aircraft observation data. The feasibility of particle effective radius retrieval from lidar ratio and backscatter ratio was simulated and studied. A method for inverting the effective radius and number concentration of atmospheric aerosols or small cloud droplets using backscatter ratio was proposed, and the error sources and applicability of the algorithm were analyzed. This algorithm was suitable for the inversion of uniformly mixed and single property aerosol layers or small cloud droplets. Compared with the previous study, this algorithm could quickly obtain the microphysical parameters of atmosphere particles and has good robustness. For aerosol particles, the inversion range that this algorithm can achieve was 0.3-1.7  $\mu\text{m}$ . For cloud droplets, it was 1.0-10  $\mu\text{m}$ . An atmosphere observation experiment was conducted using the multi-wavelength lidar developed by Xi'an University of Technology, and a thin cloud layer was captured. The microphysical parameters of aerosol and cloud during this process were retrieved. The results clearly demonstrate the growth of effective radius and number concentration.

**Key words:** Lidar; Effective radius; Gamma distribution; Aerosol; Cloud

## 1 Introduction

The vertical characteristics of aerosol and cloud are of great significance for the study of many scientific issues, such as the interaction between aerosol and cloud, the mechanism of atmospheric pollution generation, and so on (Lohmann and Feichter, 2005; Kulmala et al., 2004; Miffre et al., 2010). The high-precision detection of aerosol and cloud microphysical parameters at vertical altitude is important. At present, the main methods for obtaining atmosphere aerosol or cloud microphysical parameters include in-situ observation (He et al., 2019; Moore et al., 2021; Gao et al., 2022a; Gao et al., 2022b) and remote sensing observation (Vivekanandan et al., 2020; Johnson et al., 2009). People can obtain microphysical parameters of cloud or aerosol at vertical altitudes by mounting in-situ observation instruments on equipment such as airplanes or balloons (Kaufman et al., 1998; Cai et al., 2022), but this method has a low detection frequency and cannot obtain continuous observation data with high temporal and spatial resolution (Zhao et al., 2018). Lidar, with its advantages of high temporal and spatial resolution and high detection sensitivity, has been widely used in the field of atmosphere detection, and has important application potential in detecting optical and microphysical parameters of atmosphere aerosol and cloud (Vivekanandan et al., 2020; Hara et al., 2018; Siomos et al., 2017; Kanitz et al., 2013; Dionisi et al., 2018).

The remote sensing detection of aerosol microphysical parameters mainly uses three wavelength lidar, which can obtain four or more optical parameters (usually requiring two extinction coefficients @355 nm&532 nm and three backscatter coefficients @ 355 nm&532 nm&1064 nm) for the retrieval of aerosol microphysical parameters (Veselovskii et al., 2004; Müller et al., 1999; Veselovskii et al., 2009). The regularization algorithm (Kolgotin et al., 2023; Veselovskii et al., 2002), the principal component analysis (PCA) technique (Martin et al., 2013), and the linear estimation algorithm (Veselovskii et al., 2012) have been used for determining the aerosol bulk properties. These algorithms do not require the assumption of complex refractive index or aerosol particle size distribution (APSD), so they have been widely studied, but their applications are limited. The inversion results are unstable, and there will be good results under certain spectral types; however, in some cases, the

41 inversion error is very large. Not only that, the above methods require the complex lidar hardware systems (Di et al., 2018a;  
 42 Meskhidze et al., 2021; Müller et al., 2014). Therefore, the above algorithms cannot be well applied in most lidar systems  
 43 (most lidars in AERONET are dual wavelength), and it is necessary to establish a more reasonable method for inverting  
 44 microphysical parameters. For clouds, there are two methods used for the detection of cloud microphysical parameters. The  
 45 first method is using lidar/radar synergy for cloud microphysical parameters (Wang et al., 2002; Vivekandan et al., 2020; Zhang  
 46 et al., 2021), which can achieve the retrieval of cloud droplet with large cloud particles. For thin and sparse clouds or nascent  
 47 clouds, cloud droplet particles are usually small and cannot be detected by millimeter wave cloud radar, which affects the  
 48 application of this method. The second method is to use multiple scattering information in clouds detected by multi field of  
 49 view (FOV) or dual FOV lidar to retrieve microphysical parameters of water clouds (Wang et al. 2022). However, in order to  
 50 obtain multiple scattering signals using ground-based lidar, the larger FOV of telescope is required, which will greatly affect  
 51 daytime detection.

52 This study proposes an inversion method of atmosphere aerosol or cloud microphysical parameters based on dual  
 53 wavelength Lidar. This article mainly includes the following parts: in Section 2, we studied the APSD and cloud droplet size  
 54 distribution (CDS) measured by airborne instruments and found that they are basically consistent with the Gamma  
 55 distribution, and extract the statistical characteristics of their Gamma distribution parameters; In Section 3, the inversion  
 56 method and simulation analysis results were presented and described; In Section 4, an atmosphere observation result by lidar  
 57 was presented; Section 5 is the conclusion and discussion.

## 58 2 Gamma distribution statistical characteristics of APSD and CDS

### 59 2.1 Gamma distribution

60 The particle size distribution (Di et al., 2018a) is the variation of particle number with particle radius within a certain  
 61 radius range  $r \sim r+dr$  per unit volume, defined as

$$62 \quad n(r) = \frac{dN}{dr} \quad (1)$$

63 here,  $r$  is the particle radius,  $n(r)$  is the particle size distribution,  $N$  is the total number of particles per unit volume. The effective  
 64 radius (Di et al., 2018a) is an important parameter that characterizes the average particle size, defined as the ratio of the third-  
 65 order and second-order moments of the particle size distribution, as shown below

$$66 \quad r_{\text{eff}} = \frac{\int_{r_{\min}}^{r_{\max}} r^3 n(r) dr}{\int_{r_{\min}}^{r_{\max}} r^2 n(r) dr} \quad (2)$$

67 The most common models for APSD are Junge distribution and lognormal distribution. CDS usually described as Gamma  
 68 distribution or corrected Gamma distribution (Kolgotin et al., 2023). The Gamma function has the advantages of integrability  
 69 and recursion of various order functions. In this paper, the Gamma distribution is used to describe APSD and CDS, and  
 70 shown as

$$71 \quad n(r) dr = ar^b e^{-cr} dr \quad (3)$$

72 here,  $a$  is related to particle concentration,  $b$  is a dimensionless parameter representing shape factor, which is related to  
 73 spectral width, and  $c$  is a slope parameter.

74 In mathematics,  $\Gamma(x)$  is defined as Gamma function, and is as follow

$$75 \quad \Gamma(x) = \int_0^{+\infty} t^{x-1} e^{-t} dt, (x>0) \quad (4)$$

76 Its p-th moment of Gamma distribution can be expressed as

$$77 \quad M_p = \int_{r_{\min}}^{r_{\max}} r^p n(r) dr = \int_{r_{\min}}^{r_{\max}} r^p ar^b e^{-cr} dr = \frac{a}{c^{p+b+1}} \Gamma(p+b+1) \quad (5)$$

78 The effective radius requires second-order and third-order moments, which are

$$79 \quad M_2 = \int_{r_{\min}}^{r_{\max}} r^2 n(r) dr = \frac{a}{c^{2+b+1}} \Gamma(2+b+1) \quad (6)$$

$$80 \quad M_3 = \int_{r_{\min}}^{r_{\max}} r^3 n(r) dr = \frac{a}{c^{3+b+1}} \Gamma(3+b+1) \quad (7)$$

81 Substituting Eq. (6) and Eq. (7) into Eq. (2) yields the effective radius as follow

$$82 \quad r_{\text{eff}} = \frac{M_3}{M_2} = \frac{\int_{r_{\min}}^{r_{\max}} r^3 n(r) dr}{\int_{r_{\min}}^{r_{\max}} r^2 n(r) dr} = \frac{1}{c} \frac{\Gamma(3+b+1)}{\Gamma(2+b+1)} \quad (8)$$

83 The Gamma function has recursion, as shown in the following formula

$$84 \quad \Gamma(x+1) = x\Gamma(x) \quad (9)$$

85 According to Eq. (8) and Eq. (9), the effective radius can be simplified as

$$86 \quad r_{\text{eff}} = \frac{b+3}{c} \quad (10)$$

## 87 2.2 APSDs and CSDs in the vertical altitude

88 In order to study the characteristics of APSDs and CSDs in the vertical altitude, the APSDs and CSDs obtained from  
 89 aircraft observations by the Hebei Provincial Weather Modification Office were analyzed (from 2005 to 2006). APSDs were  
 90 measured by the PCASP-100X probe, and CSDs were obtained by the FSSP-100-ER probe (Di et al., 2018b). The PCASP-  
 91 100X is an optical particle counter for measuring aerosol size distribution from 0.10  $\mu\text{m}$  to 3.00  $\mu\text{m}$  in diameter in 15  
 92 different size bins with a frequency of 1 Hz. The sample flow volume in the PCASP-100X was set to 1  $\text{cm}^3 \text{s}^{-1}$ . FSSP-  
 93 100-ER is an instrument that measure cloud droplet size and concentration using light scattering, with the measurement  
 94 range of 0.5-47  $\mu\text{m}$ .

95 The obtained APSDs and CSDs were fitted one by one using Gamma function, and statistically analyze these fitting  
 96 parameters. In order to minimize the error at all radius, the minimization problem is solved using the following equation

$$97 \quad \int_0^{D_{\max}} \left( \log(f_m(D)) - \log(f_{\text{fitted}}(D)) \right)^2 dD \rightarrow \min \quad (11)$$

98 here,  $f_m(D)$  is the actual particle size distribution measured by the PCASP-100X,  $f_{\text{fitted}}(D)$  is the fitted distribution,  $D$  is  
 99 the aerosol particle diameter,  $D_{\max}$  is the measured maximum particle diameter. The goodness of fit  $R^2$  is used to represent  
 100 the difference between the fitting function and the measured data. The definition of goodness of fit is as follows::

$$101 \quad R^2 = 1 - \frac{\sum_{i=1}^n (y_i - \hat{y}_i)^2}{\sum_{i=1}^n (y_i - \bar{y})^2} \quad (12)$$

102 where  $y_i$  is the measured value,  $\hat{y}_i$  is the predictive value,  $\bar{y}$  is the mean measured value. The numerator represents the  
 103 sum of squared residuals, and the denominator represents the sum of squared total deviations.

104 ~3500 sets of APSDs and 2221 sets of CSDs were statistically analyzed. Over 95% of the data have a high goodness of fit  
 105 in the Gamma distribution. The goodness of fit of CSDs is higher than that of APSDs, with CSDs of 0.983 and APSDs of  
 106 0.856. The parameter  $a$  of CSDs are significantly larger than that of APSDs, and there are obvious differences of  $b$  and  $c$  for  
 107 cloud and aerosol. The literature suggests that there is a certain functional relationship between the Gamma parameters  $b$  and  
 108  $c$  of CSDs (Ding et al., 2023). Statistical analysis was conducted on the  $b$  and  $c$  parameters of APSDs and CSDs, as shown  
 109 in Fig. 1.

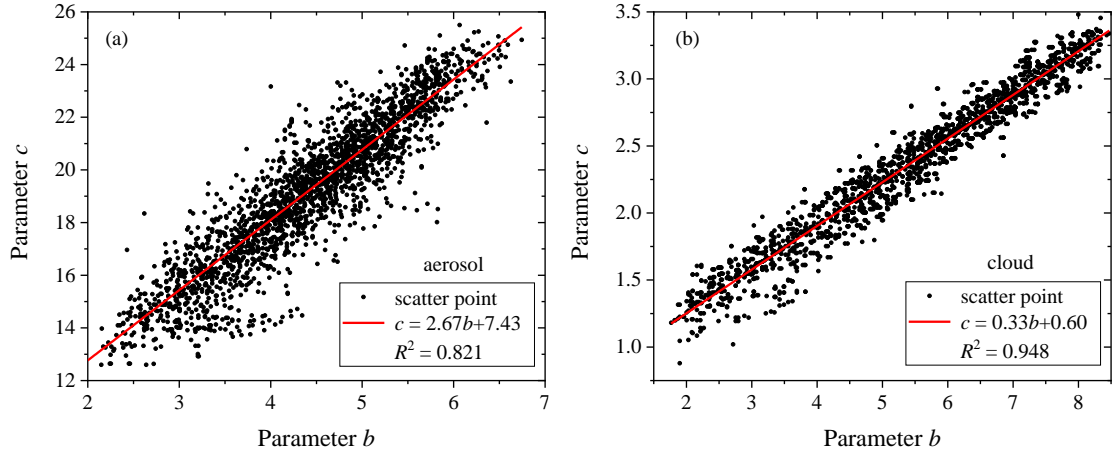


**Figure 1.** Statistical Results of parameter  $b$  and  $c$  in aerial survey data. (a) Aerosol particles, (b) cloud droplets.

According to Fig. 1, there are the remarkable linear relationships between parameter  $b$  and  $c$ . The fitting functions for CSDs and APSDs are as follows

$$\begin{cases} c_{\text{cloud}} = 0.33b_{\text{cloud}} + 0.60 \\ c_{\text{aerosol}} = 2.67b_{\text{aerosol}} + 7.43 \end{cases} \quad (13)$$

The linear relationship between the two parameters of CSDs is better with a goodness of fit of 0.948, and a linear goodness of fit of 0.821 for APSDs. According to the statistical results, the parameter  $b$  of APSDs at vertical height is mainly distributed in the range of 2-7, and CSDs is mainly distributed in the range of 2-8.

### 3. The Inversion method for microphysical parameters of atmosphere aerosols or small cloud droplets

#### 3.1 Inversion algorithm

The first step in this algorithm is the retrieval of the effective radius. The parameter  $a$  in Gamma distribution shown in Eq. (4) is related to number concentration. The ratio  $O_R(m, r)$  (lidar ratio or color ratio) of the two optical parameters can eliminate parameter  $a$ , and can be written as

$$O_R(m, r) = \frac{g_1(\lambda_1)}{g_2(\lambda_2)} \quad (14)$$

here,  $m$  is the complex refractive index of particles,  $g_1(\lambda_1)$  and  $g_2(\lambda_2)$  are the optical parameters at two wavelengths  $\lambda_1$  and  $\lambda_2$ , respectively. It can also be written as follows

$$O_R(m, r) = \frac{\int_{r_{\min}}^{r_{\max}} \pi r^2 Q_1(m, r, \lambda_1) r^b e^{-cr} dr}{\int_{r_{\min}}^{r_{\max}} \pi r^2 Q_2(m, r, \lambda_2) r^b e^{-cr} dr} \quad (15)$$

where  $Q_1$  and  $Q_2$  are the extinction efficiency factor or backscattering efficiency factor at  $\lambda_1$  and  $\lambda_2$ . Using the effective radius in the Eq. (10) instead of parameter  $c$ , the Eq. (13) can be written as follows

$$O_R(m, r_{\text{eff}}) = \frac{\int_{r_{\min}}^{r_{\max}} \pi r^2 Q_1(m, r, \lambda_1) r^b e^{-\frac{b+3}{r_{\text{eff}}} r} dr}{\int_{r_{\min}}^{r_{\max}} \pi r^2 Q_2(m, r, \lambda_2) r^b e^{-\frac{b+3}{r_{\text{eff}}} r} dr} \quad (16)$$

According to the Eq. (11) and Eq. (14), if the ratio of optical parameters monotonically changes with the effective radius, the effective radius can be obtained from the ratio of optical parameters, and then parameters  $b$  and  $c$  can also be obtained according to Eq. (11). The ratio here can be chosen as the ratio of backscatter or extinction coefficient of two wavelengths (color ratio) or the ratio of extinction coefficient of one wavelength to backscatter coefficient (lidar ratio).

After obtaining  $b$  and  $c$ ,  $a$  can be derived from the Eq. (15), written as

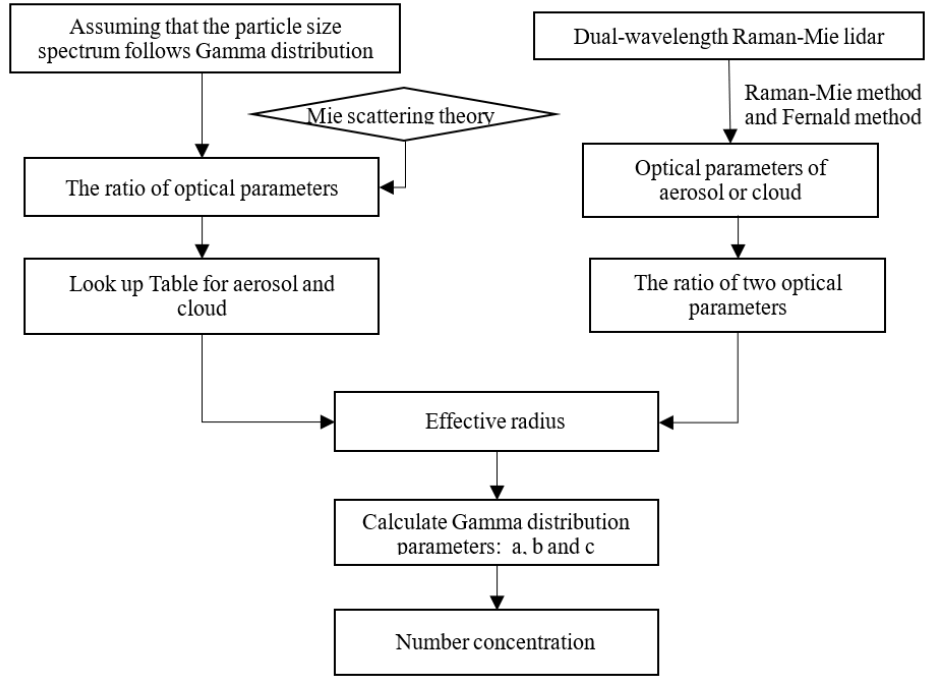
135

$$a = \frac{\int_{r_{\min}}^{r_{\max}} \pi r^2 Q_1(m, r, \lambda_1) a r^b e^{-cr} dr}{\int_{r_{\min}}^{r_{\max}} \pi r^2 Q_1(m, r, \lambda_1) r^b e^{-cr} dr} = \frac{g_1(\lambda_1)}{\int_{r_{\min}}^{r_{\max}} \pi r^2 Q_1(m, r, \lambda_1) r^b e^{-cr} dr} \quad (17)$$

136

and then, the number concentration  $N$  can be calculated by integrating the Eq. (4). The algorithm flowchart is shown below

137



138

139

**Figure 2.** The algorithm flowchart for atmosphere particle microphysical parameters.

140

The algorithm is described as follows:

141

In this algorithm, the first step is to establish a lookup table between aerosol/cloud optical parameters and microphysical parameters. 1) Assuming that aerosol particles and cloud droplets follow the Gamma distributions, calculate the extinction coefficient and backscatter coefficient at different laser wavelengths (355nm and 1064nm in this paper) based on the Mie scattering theory; 2) Calculate the ratio of backscatter coefficients for two wavelengths, which is the backscatter color ratio, or calculate the ratio of extinction coefficient to backscatter coefficient, which is the radar ratio; 3) Change the parameters of the aerosol to obtain the gamma distributions with effective radius from 0.2  $\mu\text{m}$  to 3  $\mu\text{m}$ , calculate the optical parameters and corresponding optical parameter ratios (radar ratio or backscatter color ratio) for each Gamma distribution, and establish the lookup table for aerosol effective radius; 4) Similar to the step 3, establish the lookup table for cloud drops (effective radius are from 0.5  $\mu\text{m}$  to 5  $\mu\text{m}$ ). After the lookup table is completed, the microphysical parameters of aerosols or clouds are calculated based on the lookup tables and LiDAR detection data. The specific steps are as follows: 1) the dual-wavelength (355 nm and 1064 nm) Raman LiDAR need be selected for the detection of atmosphere; 2) Raman and Fernald methods are used for the retrieval of optical parameters at multi-wavelengths, and the backscatter color ratio or lidar ratio can be obtained ; 3) aerosol and cloud layers are identified based on lidar echo signals; 4) Retrieve the effective radius of aerosols or cloud droplets at different heights based on optical parameters ratios and lookup tables; 5) Calculate the parameters b and c in the Gamma distribution according to formulas (13) and (16); 6) Calculate the value of a in the Gamma distribution according to the Eq.(17); 7) Calculate the number concentration according to the Eq. (3).

158

### 3.2 The simulation

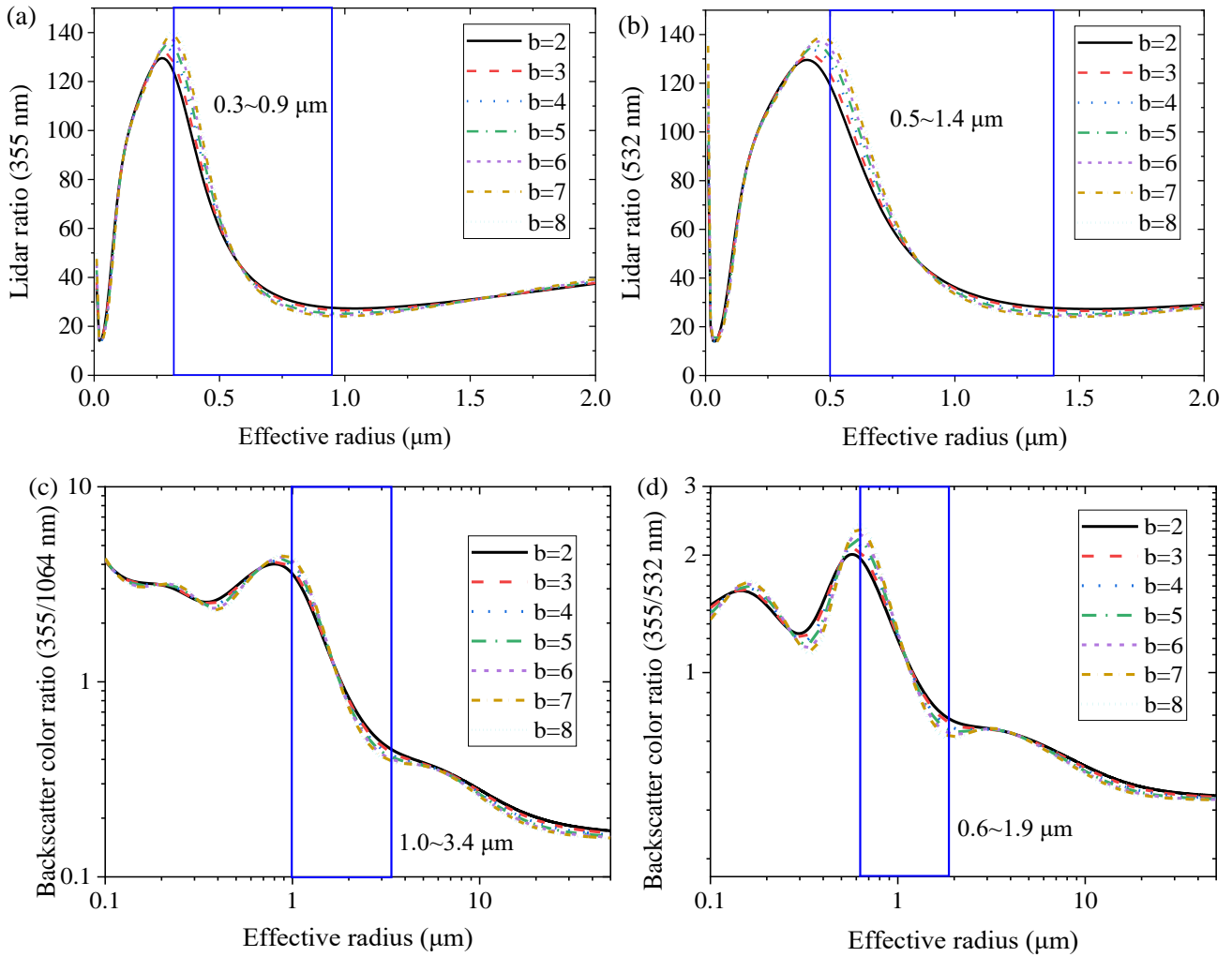
159

#### 3.2.1 The relationship between lidar ratio, color ratio, and effective radius

160

Due to the different complex refractive indices of aerosols and clouds, we will discuss them separately. Water clouds are

161 composed of liquid droplets, the complex refractive index of  $1.33-10^{-7}i$  was selected. The theoretical relationship curves of  
 162 lidar ratio of 355 nm, lidar ratio of 532 nm, 355/1064 nm backscatter color ratio, 355/532 nm backscatter color ratio with  
 163 effective radius were calculated and shown in Fig. 3(a) to 3(d).

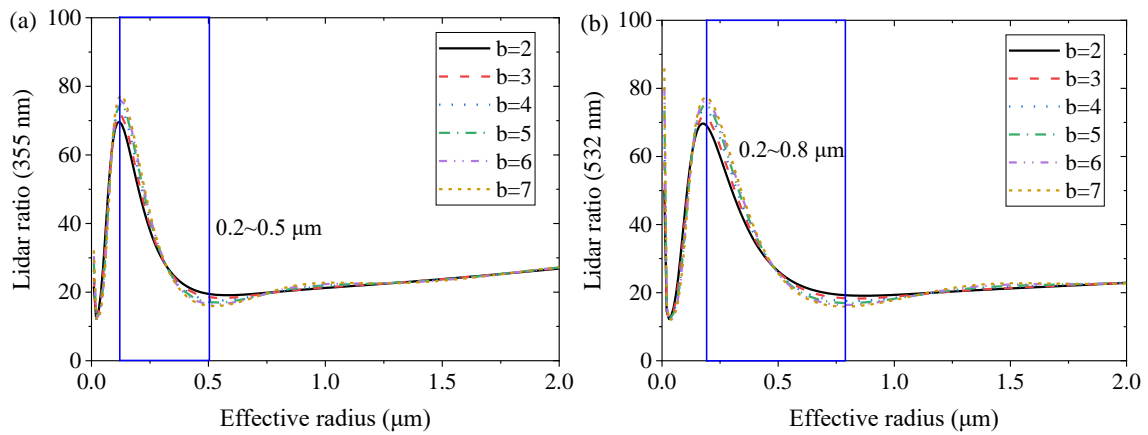


164

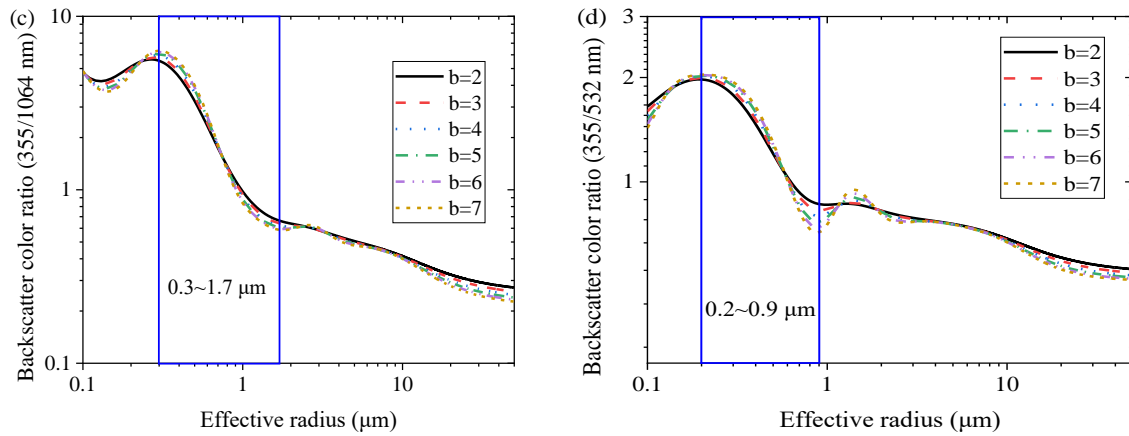
165

166 **Figure 3.** The theoretical relationship curves of colour ratio or lidar ratio with effective radius,  $m=1.33-0.10^{-7}i$ . (a) Lidar ratio of 355 nm,  
 167 (b) lidar ratio of 532 nm, (c) the ratio of backscatter coefficients (355/1064 nm), (d) the ratio of backscatter coefficients (355/532 nm).

168 The composition of aerosols is complex, with a large variation of complex refractive index, ranging from 1.33 to 1.70 in the  
 169 real part and 0 to 0.05 in the imaginary part. Assuming the complex refractive index of aerosols is  $1.47-0.002i$ , Fig. 4(a) to 4(d)  
 170 respectively show the theoretical relationship curves of aerosol when parameter  $b$  is set to 2-7.



171



172

173

174

175

176

177

178

179

180

181

182

183

184

185

**Figure 4.** The theoretical relationship curves of colour ratio or lidar ratio with effective radius,  $m=1.47-0.002i$ . (a) Lidar ratio of 355 nm, (b) lidar ratio of 532 nm, (c) the ratio of backscatter coefficients (355/1064 nm), (d) the ratio of backscatter coefficients (355/532 nm).

The blue boxes in Figures 3 and 4 refer to the monotonic variation intervals of aerosols and cloud droplets, respectively. As shown in the figures, when the complex refractive index is constant and the parameter  $b$  is set to 2-7 or 2-8, the corresponding curve trend is consistent. Under a constant complex refractive index, parameter  $b$  does not change the trend of the curve. The change of  $b$  has little effect on the curve. If the color ratio (355 nm/1064 nm) is selected for the retrieval of effective radius, the influence of  $b$  value on the results is about 5% (as shown in Figure 3c and 4c). If the lidar ratio is selected for the retrieval of effective radius, the influence of  $b$  value on the results will be slightly greater, and it might reach  $\sim 10\%$  (as shown in Figure 3a and 4a). Within the monotonic interval, the effective radius of particles can be retrieved from the curves. The monotonic interval varies with optical parameter. It can be seen that whether it is clouds or aerosols, the monotonic range of the backscatter color ratio is the widest, as shown in Fig. 3(c) and Fig. 4(c). The larger the value of  $b$ , the more pronounced the Gamma function describes the characteristics of large particles. Therefore, in the subsequent inversion,  $b=6$  is taken for cloud droplets, and  $b=3$  for aerosols.

186

187

188

189

190

191

192

193

194

195

196

Considering the laser's penetration ability, and the monotonic range of optical parameter ratios with effective radius shown in Fig. 3 and Fig. 4, the backscatter ratio of 355 nm/1064 nm for the inversion is the optimal choice. According to Fig. 3(c), the effective radius that can be retrieved using backscatter ratio of 355 nm/1064 nm is above 1  $\mu\text{m}$ . The optimal inversion range is 1-3.4  $\mu\text{m}$ , and the maximum inversion radius can reach 10  $\mu\text{m}$ . For aerosol particles, the theoretically retrieval effective radius is above 0.3  $\mu\text{m}$ , the optimal inversion interval is 0.3-1.7  $\mu\text{m}$ . The applicability of this algorithm is limited, and it is applicable for aerosols and small cloud droplets. For aerosols, particle diameter is usually 0.01~10  $\mu\text{m}$ , while the effective particle radius ranges from 0.3  $\mu\text{m}$  to 1.2  $\mu\text{m}$  for urban aerosols (This is calculated based on ground and aircraft observation data.). Usually, water droplets diameter larger than 2 microns are called cloud droplets. Therefore, this algorithm is suitable for the detection of urban aerosols and small cloud drops. The above curves in Fig. 3 and Fig. 4 obtained are calculated using Mie scattering theory and are suitable for spherical particles. The spherical particles in the atmosphere can be distinguished from the depolarization ratio.

197

### 3.2.2 The influence of complex refractive index on the backscatter color ratio

198

199

When the complex refractive index changes and  $b$  is 3, the backscatter color ratios of the 355 nm and 1064 nm wavelengths are shown in Fig. 5(a) to 5(d).

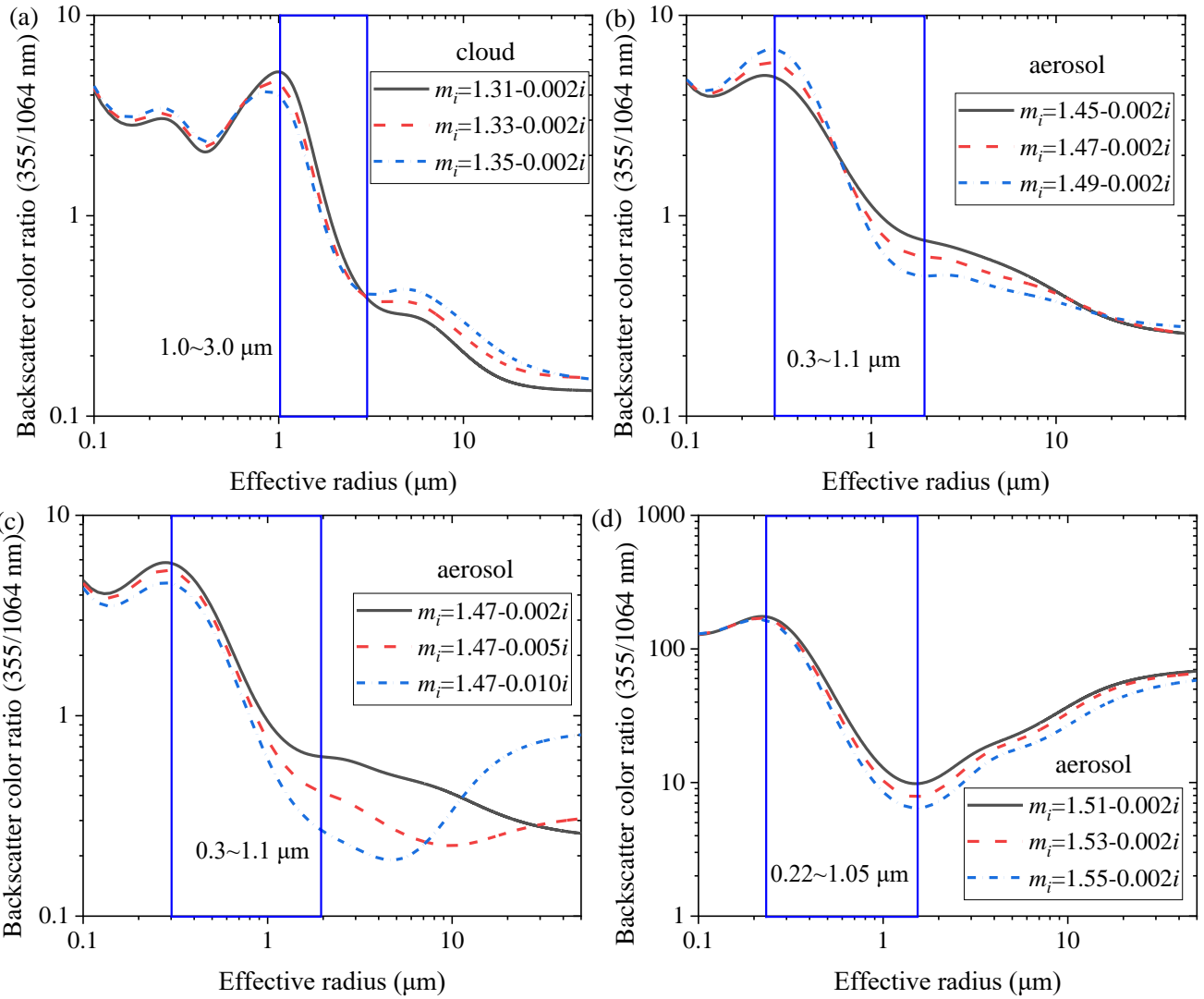


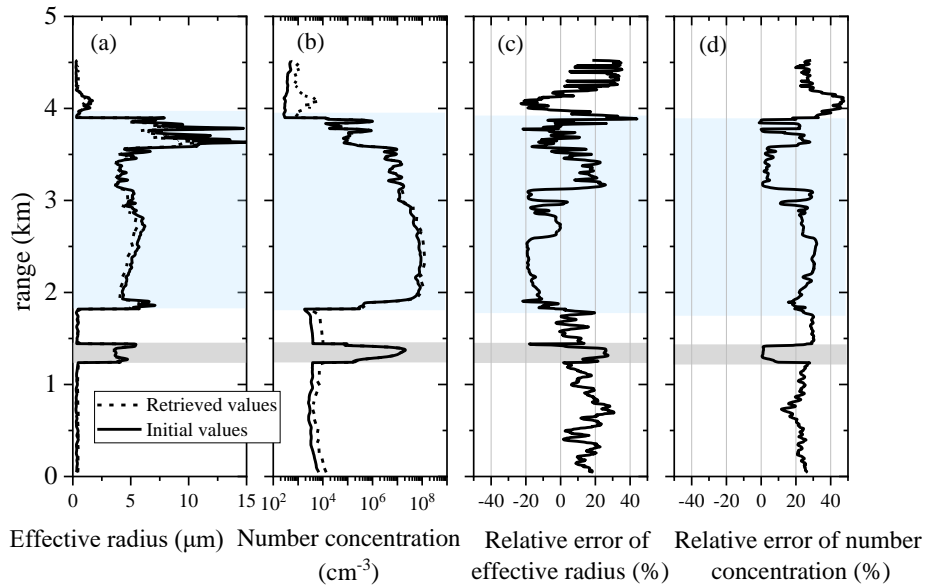
**Figure 5.** The color ratio with different complex refractive indices. (a) Aerosol with different real part of complex refractive index (real part < 1.50), (b) aerosol with different imaginary part of complex refractive index (real part < 1.50), (c) aerosol with different real part of complex refractive index (real part > 1.50), (d) aerosol with different imaginary part of complex refractive index (real part > 1.50).

According to Fig. 5, when the complex refractive index of particles changes, the color ratio curves will fluctuate, but they always monotonically decrease from 0.3  $\mu\text{m}$  to 1  $\mu\text{m}$ . Therefore, if the aerosol composition is stable, the color ratio curve can well reflect the trend of effective radius variation.

### 3.2.3 Algorithm verification

The verification of this algorithm is achieved through simulation. The specific steps are as follows: 1) Calculate the effective radius and number concentration using APSD and CDSO observed by aircraft and the equation (8); 2) Calculate the backscatter coefficient at two wavelengths of 355 nm and 1064 nm, and then calculate the color ratio according to the Eq. (13); 3) According to the color ratio and the algorithm described in Figure 2 of Section 3.1, the effective radius and number concentration profiles can be retrieved; 4) Compare the effective radius and numerical concentration in steps 2) and 4), as shown in Fig. 6, to verify the algorithm inversion.





215

216

217

**Figure 6.** Simulation and verification of the algorithm with aircraft data. (a) effective radius, (b) number concentration, (c) effective radius error, (d) number concentration error.

218

219

220

221

222

223

224

225

Figure 6(a) and 6(b) are the true values and inversion results of the effective radius and number concentration of an aircraft observation at vertical altitude, respectively. Figure 6(c) and 6(d) show the relative errors, respectively. The light gray and light blue shaded areas in the figures are cloud layers. It can be seen that effective radius and number concentration can be well retrieved using the algorithm. Figure 6 shows that the retrieval error of cloud droplets is relatively small, within  $\pm 20\%$  and  $\pm 30\%$  for effective radius and number concentration. The errors are  $\pm 20\%$  and  $\pm 40\%$  for aerosol. The inversion error of microphysical parameters of aerosol particles is larger than that of cloud droplets. The reasons are: 1) aerosol types are more complex, and the assumption of complex refractive index is prone to deviation; 2) APSDs is more complex than CSDs, and the adaptability to Gamma distribution is relatively low.

226

### 3.3 Error analysis of the algorithm

227

228

229

The inversion errors of effective radius and number concentration mainly come from three aspects: 1) error introduced by non-spherical particles; 2) error introduced by the assumption of Gamma distribution; 3) error introduced by improper assumption of complex refractive index; 4) error caused by optical parameter inversion deviation.

230

231

232

233

234

235

236

237

238

For urban aerosols and water clouds, their particles are spherical, so the error caused by non-spherical particles can be ignored. The error introduced by the assumption of Gamma distribution is relatively complex and difficult to accurately calculate. This study evaluates this error by numerical simulation based on APSDs and CSDs data by aircraft observations. Actually, the error presented in Fig. 6 is mainly caused by the assumption of Gamma distribution. Calculate optical parameters of over 5000 sets of APSDs and CSDs data, and retrieve the microphysical parameters using our algorithm. The calculated standard deviations between the inversion results and the actual data are: for aerosols, the standard deviation of the effective radius is  $\sim 10\%$ , and the standard deviation of numerical concentration is  $\sim 20\%$ ; For clouds, the standard deviation of the effective radius is  $15\%$ , and the standard deviation of numerical concentration is  $\sim 20\%$ .

239

240

241

242

243

244

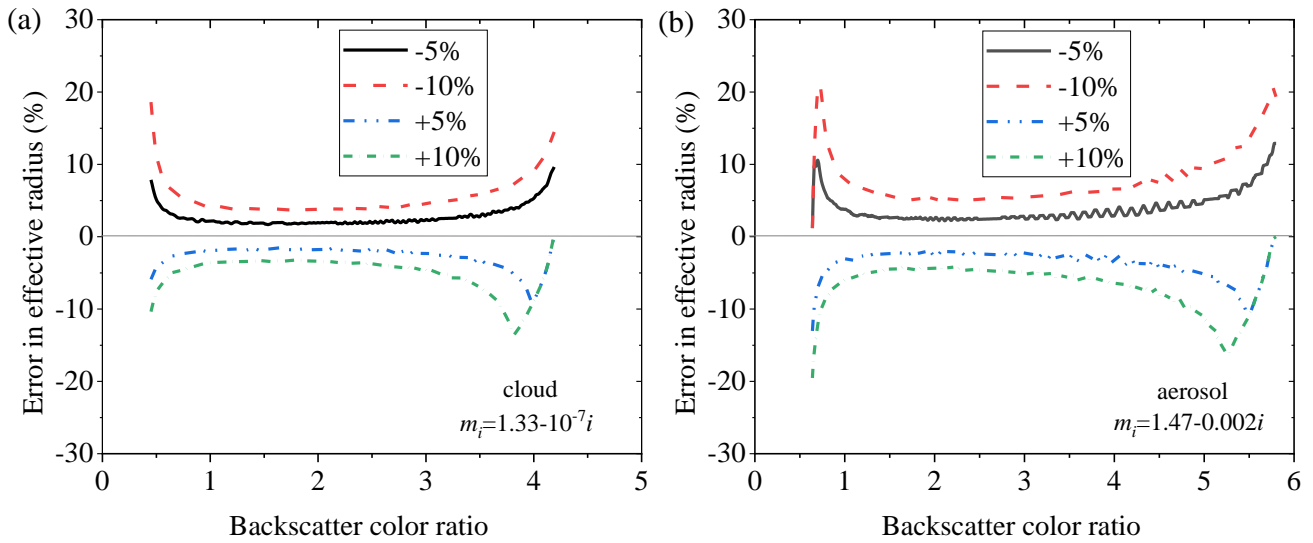
245

246

The deviation introduced by improper assumption of complex refractive index may be the largest term in this technique. For water clouds, the complex refractive index is stable and the deviation caused by it can be ignored. It is difficult to accurately obtain the complex refractive index of aerosols, and the deviation caused by the complex refractive index may reach over  $100\%$ . Figure 6 shows the effect of complex refractive index variation on the optical parameter ratio. From Figure 6, it can be seen that when the real part of the complex refractive index changes within the range of  $0.03$  and the imaginary part changes within  $0.01$ , the effective radius deviation caused by the complex refractive index is within a controllable range. After calculation, the deviation does not exceed  $40\%$ . And it can be seen that although complex refractive index can lead to the significant change of the effective radius value, when the aerosol is constant,

247 its monotonic characteristics remain unchanged, which means that the evaluation of particle size changes is reliable.

248 In order to quantitatively analyze the impact of optical parameter errors on the effective radius inversion results, the effective  
 249 radius errors caused by color ratio error were calculated when they are  $\pm 5\%$  and  $\pm 10\%$ , and shown in Fig. 7.



250

251 **Figure 7.** Errors in effective radius in Look-Up-Table when there are  $\pm 5\%$  and  $\pm 10\%$  errors in the backscatter color ratio. (a) Cloud  
 252 droplets, (b) aerosol particles.

253 From Fig. 7 (a), it can be seen that when there are errors of  $\pm 5\%$  and  $\pm 10\%$  in the backscatter color ratio, the inversion errors  
 254 of the effective radius of cloud droplets are within  $\pm 10\%$  and  $\pm 20\%$ , respectively. According to Fig. 7(b), when there are errors  
 255 of  $\pm 5\%$  and  $\pm 10\%$ , the inversion errors of aerosol effective radius are within  $\pm 20\%$  and  $\pm 30\%$ , respectively.

256 Considering the actual inversion ability of LiDAR, the deviation of color ratio will reach 10%. The above errors are  
 257 independent of each other. The final evaluation shows that the mean square deviation of the inversion error of aerosol  
 258 effective radius is less than 45%, and the standard deviation of the inversion error of cloud droplet effective radius is less  
 259 than 25%.

260 The inversion error of number concentration comes from the final superposition of optical parameter error and effective  
 261 radius error, and the error should be slightly larger than effective radius. In this algorithm, the complex refractive index needs  
 262 to be assumed. The physical and chemical properties of aerosol particles and cloud droplet particles that interact with the cloud  
 263 are similar, with a complex refractive index similar to that of the cloud. Continuous microphysical parameter profiles can be  
 264 obtained by this algorithm. For the uniformly mixed aerosol layer, it can be considered that the complex refractive index within  
 265 the layer remains unchanged. Therefore, this algorithm is suitable for the inversion of microphysical parameters of uniformly  
 266 mixed aerosol particles and small cloud droplet particles.

## 267 4 Experiment

### 268 4.1 Instrument

269 A multi-wavelength (355 nm/532 nm/1064 nm) lidar has been developed in Xi'an University of Technology (XUT). A  
 270 Cassegrain telescope is employed as the optical receiver, and narrowband interference filters are utilized as core filter devices  
 271 to finely separate the backscatter signals. The system consists of five detection channels: the two elastic scattering channels at  
 272 the wavelength of 355 nm and 1064 nm, the nitrogen Raman scattering channel at 387 nm, and the two polarization channels  
 273 at 532 nm. Table 1 summarizes the main system parameters of the lidar system.

274

**Table 1.** System parameters of multi-wavelength Raman-Mie scattering Lidar.

Instrument	Main instrument parameters	
	Wavelength of laser	355 nm, 532 nm, 1064 nm
	Light source	Leibao SGR series Nd: YAG pulsed laser

Multi-wavelength Raman-Mie Scattering Lidar		Pulse width	8.4 ns	Repetition frequency	10 Hz
		Laser divergence angle	$\leq 0.5$ mrad		
	Telescope	Cassegrain telescopes			
		Focal length	2 m	Field of view	0.5 mrad
		Aperture	400 mm		
	Wavelength of signal	355 nm (Mie channel), 387 nm (Raman channel), 532 nm (Polarization channel), 1064 nm (Mie channel)			
	Time resolution	2 min			
Distance resolution	3.75 m				

275

276

277

278

279

The optical parameters obtained from this system are the backscatter coefficients at 355 nm ( $\beta_{355}$ ) and 1064 nm ( $\beta_{1064}$ ), extinction coefficient of 355nm ( $\alpha_{355}$ ), depolarization ratio of 532 nm ( $\delta_{532}$ ).  $\beta_{355}$  is obtained by inverting the Mie-scattering and Raman channel without assuming lidar ratio.  $\beta_{1064}$  can be inverted by the Fernald method, as described in Wang et al (2023a) and Li et al (2016).

280

## 4.2 The experimental observation of cloud layer

281

### 4.2.1 The experimental observation

282

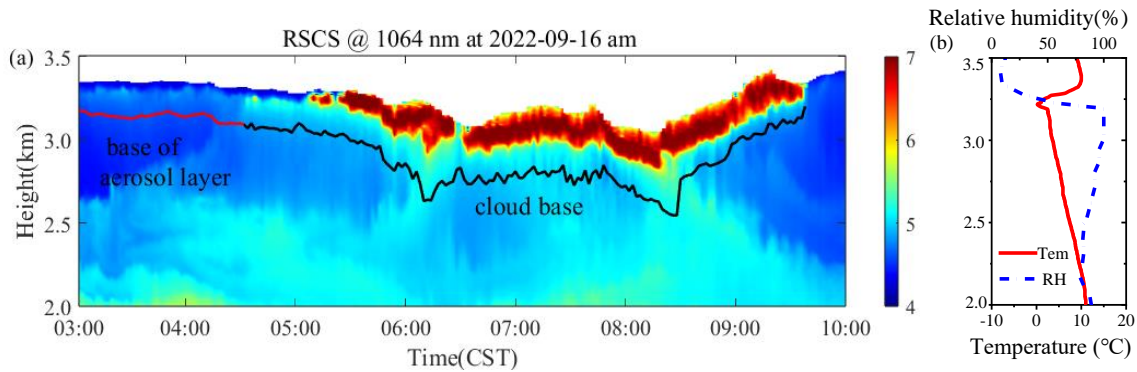
283

284

285

286

Experimental observations were performed based on the lidar of XUT at the Jinghe National Basic Meteorological Observing Station (34.43°N, 108.97°E) on September 16, 2022 (BJT). The observation experiment lasted for 7 hours with a time resolution of 2 minutes. Figure 8(a) shows the Time Height Intensity (THI) of the Mie-Rayleigh signal at 1064 nm, and the color bar values in the figure are the logarithm of RSCS. Figure 8(b) are the temperature and relative humidity profiles obtained from the sounding balloon at 7:15 am.



287

288

289

**Figure 8.** Lidar and sounding balloon observations. (a) THI diagram of RSCS at 1064 nm observed by lidar at 03:00-10:00 September 16, 2022(CST), (b) temperature and relative humidity observed by sounding balloon at 07:15 September 16, 2022.

290

291

292

293

294

295

According to Fig. 8(a), there are signals changing from weak to strong above the black curve near 3 km. After 5:00, the echo signal gradually increased and the laser could not penetrate. The red and black lines in the figure correspond to the lower boundaries of the aerosol layer and cloud layer of interest, respectively, calculated by differential zero crossing method. According to the temperature and humidity profiles shown in Fig. 8(b), the temperature below 3.5 km is higher than 0°C, and the relative humidity reaches over 90% at 3 km-3.2 km. Therefore, it can be determined that the strong signal appearing near 3 km in the atmosphere is water cloud.

296

### 4.2.2 The optical and microphysical parameter profiles

297

298

299

300

301

302

Figure 9 shows the observed signals of the lidar experiment near 5 o'clock on September 16, 2022, as well as the retrieved optical and microphysical parameters. Figure 9(a) is the dual wavelength RSCS with enhanced signal in the cloud, especially at 1064 nm. Figure 9(b) shows the volume depolarization ratio profile. The volume depolarization ratio in aerosols and clouds is less than 0.05, indicating that the detected aerosols and clouds are spherical particles. Figure 9(c) show the dual wavelength backscattering coefficient profiles at 355 nm and 1064 nm, while Fig. 9(d) is the ratio of backscattering coefficients at 355 nm and 1064 nm, i.e., backscatter color ratio (Wang et al., 2023b).

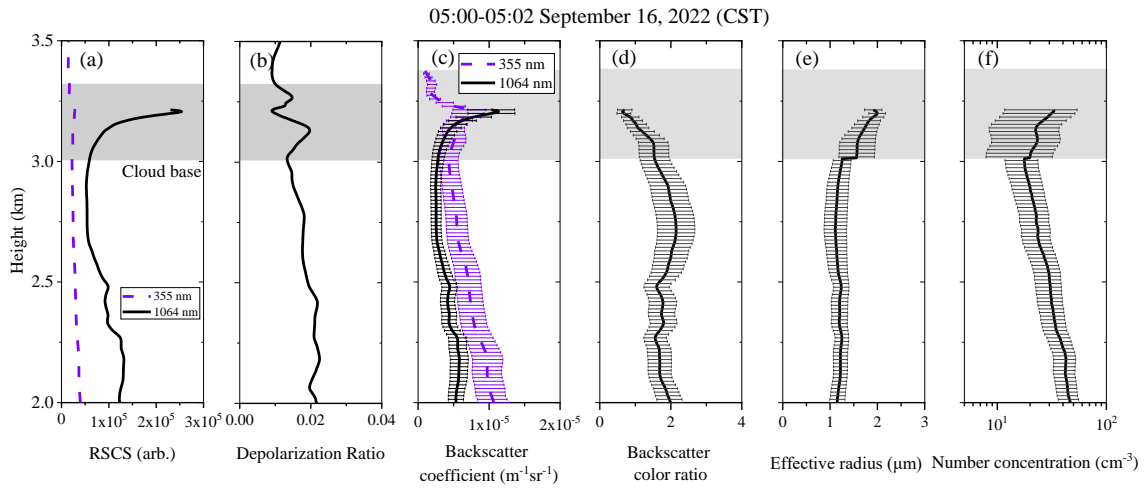
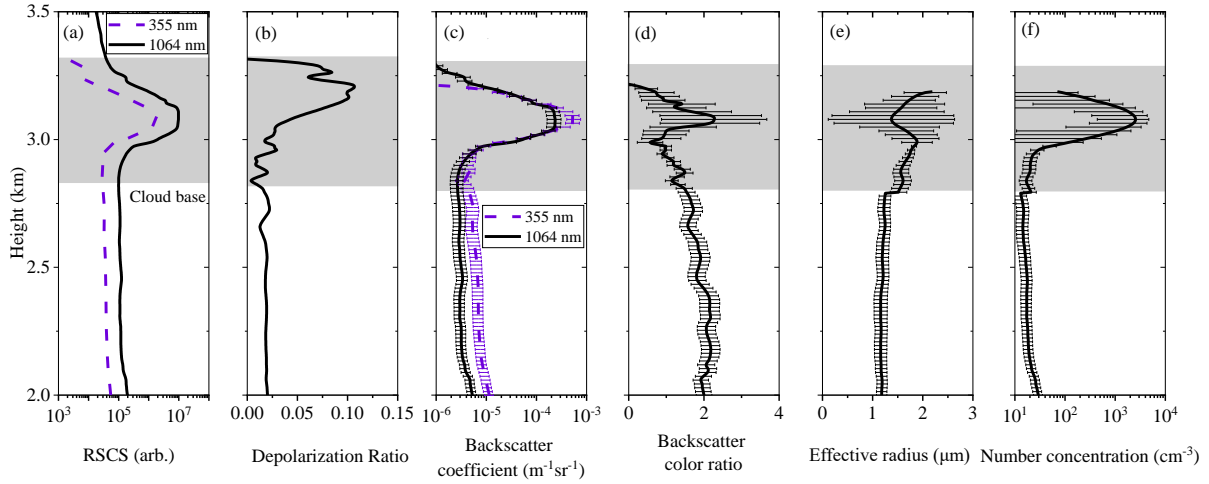


**Figure 9.** Lidar observation results at 05:00-05:02 September 16, 2022(CST). (a)Dual-wavelength RSCSs, (b)depolarization ratio, (c)backscatter coefficients, (d)backscatter color ratio, (e)effective radius, (f)number concentration.

The depolarization ratio of aerosols below the cloud layer does not change significantly, indicating that aerosols are uniformly mixed. Based on the inversion algorithm, the effective radius and number concentration profiles are calculated, as shown in Fig. 9(e) and 9(f), respectively. In the process of cloud shown in Figure 8, the aerosol hygroscopicity increase plays an important role. According to Figure 8b, the relative humidity reaches 100% near 3km, and below 3km, the relative humidity is less than 100%. Therefore, the aerosol lookup table is used below the cloud base for the retrieval of aerosol profiles, and the cloud droplet lookup table is used above the cloud base (gray shaded area). The effective radius of aerosols under cloud layer ranges from 1.1 to 1.3  $\mu\text{m}$ , and the concentration fluctuates between 17 and 60  $\text{cm}^{-3}$ , and the values decrease with increasing height. At the cloud base, the effective radius reaches 1.6  $\mu\text{m}$ , and the concentration is 20  $\text{cm}^{-3}$ . As the height above the cloud base increases, the effective radius and number concentration both show an increasing trend. The error bars in Fig. 9 represent the uncertainty of the inversion result. The error of backscattering coefficient and backscatter color ratio is determined by the signal-to-noise ratio of the LiDAR system and the error of the optical parameter inversion algorithm. The error bar of the effective radius represents the uncertainty of the results caused by optical parameter errors and gamma distribution assumption errors.

Figure 10 shows the observed signals of the lidar experiment at 7:20 on September 16, 2022, as well as the retrieved optical and microphysical parameters. Compared with Figure 9, RSCS (Fig. 10(a)) and backscatter coefficients (Fig. 10(c)) in the cloud layer increases significantly. From Fig. 10(b), the depolarization ratio increases above 3.2 km, and it should be caused by multiple scattering or low signal-to-noise ratio. The effective radius and numerical concentration of aerosols under the clouds in Fig. 10 show little change compared to Fig. 9. The number concentration in the clouds shown in Fig. 10(f) has significantly increased, reaching  $\sim 2000 \text{ cm}^{-3}$ , but the effective radius didn't change obviously, about 1-2  $\mu\text{m}$ , see Fig. 10(e). According to Fig. 8 (b), it can also be observed that there is a significant inversion layer at 3.2 km, so it is normal for there to be more aerosol accumulation below the inversion layer.

07:20-07:22 September 16, 2022 (CST)



328

329

330

**Figure 10.** Lidar observation results at 07:20-07:22 September 16, 2022(CST). (a)Dual-wavelength RSCSs, (b)depolarization ratio, (c)backscatter coefficients, (d)backscatter color ratio, (e)effective radius, (f)number concentration.

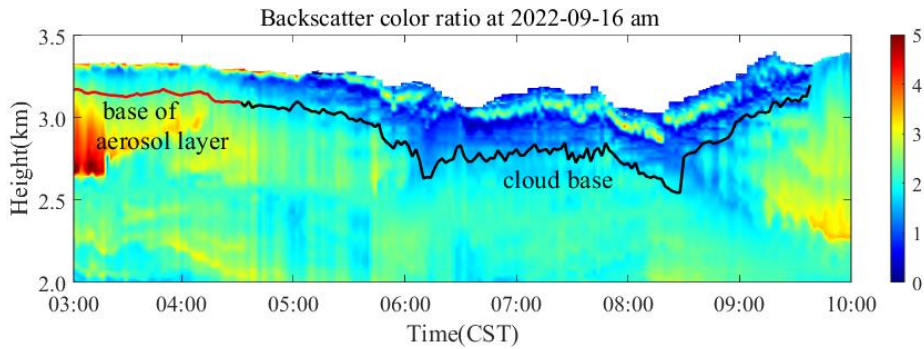
331

### 4.3 the observation results of cloud process

332

333

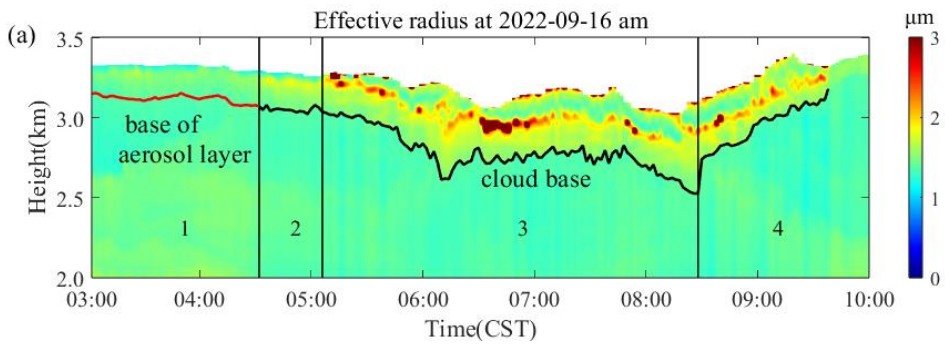
Figure 11 shows the THI of color ratio. In the region with cloud, the color ratio is relatively small, about 0.5-2, and the color ratio of aerosols is relatively large, about 2-7.



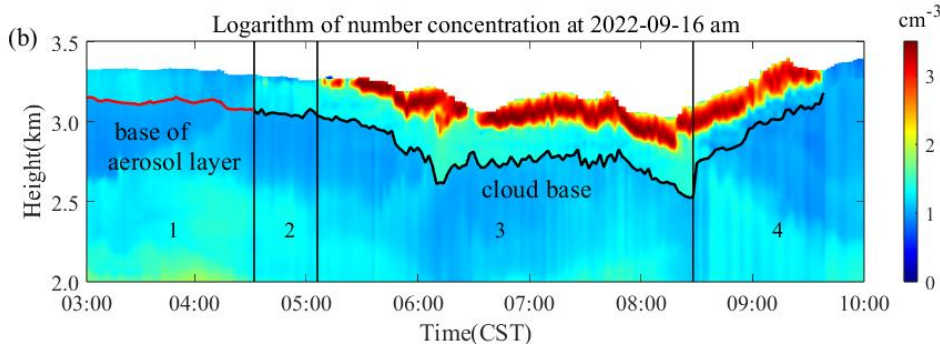
334

335

**Figure 11.** Inversion results of backscatter color ratio at 03:00-10:00 September 16, 2022(CST).



336



337

338 **Figure 12.** Microphysical parameters inversion results of atmospheric particulate matters at 03:00-10:00 September 16, 2022(CST).

339 (a)Effective radius, (b)number concentration.

340 Figure 12 shows the changes of effective radius and particle number concentration (displayed in logarithmic form). The  
341 observation results can be separated into four stages, marked with “1/2/3/4” in Fig. 12. There are no clouds in regions 1 and 2,  
342 but based on the lidar echo signal, we can see a more obvious signal growth and change process. Stage 1: From 03:00 to 04:30,  
343 clouds have not yet formed, but an obvious layer of aerosol at 3.2 km with an average thickness of 180 m can be seen. The  
344 effective radius and number concentration are relatively small, ranging from 1.2 to 1.5  $\mu\text{m}$  and from 8.5  $\text{cm}^{-3}$ -20.6  $\text{cm}^{-3}$ . Stage  
345 2: 04:30-05:06, during which the echo signal of the lidar is enhanced, the particles radius increase, and the effective radius  
346 increases to 1.4-1.8  $\mu\text{m}$ . The concentration range is 13.3  $\text{cm}^{-3}$ -25.6  $\text{cm}^{-3}$ . Stage 3: From 05:00 to 08:30, cloud droplets  
347 generated and cloud layer appeared. The echo signal intensifies sharply, and the effective radius and number concentration  
348 increase significantly, with the effective radius of 1.5-5.3  $\mu\text{m}$  and the concentration of 18.7  $\text{cm}^{-3}$ -2853.5  $\text{cm}^{-3}$ . Due to the  
349 increase of number concentration, the laser cannot penetrate the cloud layer. Stage 4: From 08:30 to 10:00, the cloud layer  
350 rises and the cloud base height increases from 2.5 km to 3.27 km. The effective radius inside the cloud remains unchanged,  
351 but the numerical concentration decreases. At 9:40, the cloud signal disappeared, possibly due to the cloud leaving the field of  
352 view of lidar and unable to be observed.

## 353 5. Conclusion and Discussion

354 This study proposes a method to estimate the microphysical parameters of atmosphere aerosols and small cloud droplets  
355 using two optical parameters. Assuming Gamma distribution, the effective radius and number concentration of aerosols or  
356 small cloud droplets can be calculated using the backscatter color ratios of 355nm and 1064nm wavelengths. An atmosphere  
357 observation experiment was conducted using the multi-wavelength Lidar, and the effective radius and number concentration  
358 were retrieved. The results indicate that the algorithm is stable and reliable.

359 This algorithm has simple hardware requirements for lidar, requiring only two wavelengths to achieve the retrieval of  
360 microphysical parameters. At the same time, the algorithm is simple, and can obtain stable data inversion results. It is suitable  
361 for the retrieval of cloud droplet generation process and aerosol with uniform mixing and relatively stable composition. The  
362 limitation of this algorithm is that it requires assuming the complex refractive index of particles. The complex refractive index  
363 of aerosols varies greatly, and incorrect assumptions about the complex refractive index can have a certain impact on the results.  
364 Furthermore, this algorithm is not applicable for retrieval of large particle sizes (radius>10  $\mu\text{m}$ ). To detect larger particle sizes,  
365 millimeter wave cloud radar and lidar can be used for joint observation. We will carry out this work in the future.

## 366 Data availability

367 The data and codes related to this article are available upon request from the corresponding author.

## 368 Author contributions

369 Conceptualization: Huige Di

370 Investigation: Xinhong Wang & Huige Di

371 Methodology: Huige Di & Xinhong Wang

372 Software: Xinhong Wang & Ning Chen

373 Writing — original draft: Xinhong Wang & Huige Di

374 Writing — review & editing: Huige Di, Dengxin Hua

375 Supervision: Huige Di & Jing Guo

376 Data collation: Wenhui Xin, Shichun Li, Yan Guo, Qing Yan, & Yufeng Wang

377 Project administration: Huige Di & Dengxin Hua

378 **Competing interests**

379 The authors declare that they have no conflicts of interest related to this work.

380 **Acknowledgements**

381 We express our gratitude to the Xi'an Meteorology Bureau of Shaanxi Province, Xi'an, Mei Cao for providing the relevant  
382 supporting data.

383 **Financial support**

384 This research was supported by the National Natural Science Foundation of China, the Innovative Research Group  
385 Project of the National Natural Science Foundation of China (Grant Nos. 42130612).

386 **Reference**

387 Cai, Z. X., Li, Z. Q., Li, P. R., Li, J. X., Sun, H. P., Yang, Y. M., Gao, X., Ren, G., Ren, R. M., and Wei, J.: Vertical  
388 Distributions of Aerosol and Cloud Microphysical Properties and the Aerosol Impact on a Continental Cumulus Cloud Based  
389 on Aircraft Measurements from the Loess Plateau of China, *Atmos. Environ.*, 270, 118888,  
390 <https://doi.org/10.1016/j.atmosenv.2021.118888>, 2022.

391 Ding, J. F., Tian, W. S., Xiao, H., Cheng, B., Liu, L., Sha, X. Z., Song, C., Sun, Y., and Shu, W. X.: Raindrop size  
392 distribution and microphysical features of the extremely severe rainstorm on 20 July 2021 in Zhengzhou, China, *Atmos. Res.*,  
393 289, 106739, <https://doi.org/10.1016/j.atmosres.2023.106739>, 2023.

394 Dionisi, D., Barnaba, F., Diémoz, H., Di Liberto, L., and Gobbi, G. P.: A multiwavelength numerical model in support  
395 of quantitative retrievals of aerosol properties from automated lidar ceilometers and test applications for AOT and PM10  
396 estimation, *Atmos. Meas. Tech.*, 11, 6013-6042, <https://doi.org/10.5194/amt-11-6013-2018>, 2018.

397 Di, H. G., Wang, Q. Y., Hua, H. B., Li, S. W., Yan, Q., Liu, J. J., Song, Y. H., and Hua, D. X.: Aerosol Microphysical  
398 Particle Parameter Inversion and Error Analysis Based on Remote Sensing Data, *Remote Sens.*, 10, 1753,  
399 <https://doi.org/10.3390/rs10111753>, 2018a.

400 Di, H. G., Zhao, J., Zhao, X., Zhang, Y. X., Wang, Z. X., Wang, X. W., Wang, Y. F., Zhao, H., and Hua, D. X.:  
401 Parameterization of aerosol number concentration distributions from aircraft measurements in the lower troposphere over  
402 Northern China, *J. Quant. Spectrosc. Ra.*, 218, 46-53, <https://doi.org/10.1016/j.jqsrt.2018.07.009>, 2018b.

403 Gao, P., Wang, J., Tang, J. B., Gao, Y. Z., Liu, J. J., Yan, Q., and Hua, D. X.: Investigation of cloud droplets velocity  
404 extraction based on depth expansion and self-fusion of reconstructed hologram, *Opt. Express*, 30, 18713-18729,  
405 <https://doi.org/10.1364/OE.458947>, 2022a.

406 Gao, P., Wang, J., Gao, Y. Z., Liu, J. J., and Hua, D. X.: Observation on the Droplet Ranging from 2 to 16  $\mu\text{m}$  in Cloud  
407 Droplet Size Distribution Based on Digital Holography, *Remote Sens.*, 14, 2414, <https://doi.org/10.3390/rs14102414>, 2022b.

408 Hara, Y., Nishizawa, T., Sugimoto, N., Osada, K., Yumimoto, K., Uno, I., Kudo, R., and Ishimoto, H.: Retrieval of  
409 Aerosol Components Using Multi-Wavelength Mie-Raman Lidar and Comparison with Ground Aerosol Sampling, *Remote  
410 Sens.*, 10, 937, <https://doi.org/10.3390/rs10060937>, 2018.

411 He, Y., Sun, Y. L., Wang, Q. Q., Zhou, W., Xu, W. Q., Zhang, Y. J., Xie, C. H., Zhao, J., Du, W., Qiu, Y. M., Lei, L.,  
412 Fu, P. Q., Wang, Z. F., and Worsnop, D. R.: A Black Carbon-Tracer Method for Estimating Cooking Organic Aerosol from  
413 Aerosol Mass Spectrometer Measurements, *Geophys. Res. Lett.*, 46, 8474-8483, <https://doi.org/10.1029/2019GL084092>, 2019.

414 Johnson, B. T., Christopher, S., Haywood, J. M., Osborne, S. R., McFarlane, S., Hsu, C., Salustro, C., and Kahn, R.:

415 Measurements of aerosol properties from aircraft, satellite and ground-based remote sensing: a case-study from the Dust and

416 Biomass burning Experiment (DABEX), *Q. J. Roy. Meteor. Soc.*, 135, 922-934, <https://doi.org/10.1002/qj.420>, 2009.

417 Kanitz, T., Ansmann, A., Engelmann, R., and Althausen, D.: North-south cross sections of the vertical aerosol distribution

418 over the Atlantic Ocean from multiwavelength Raman/polarization Lidar during Polarstern cruises, *J. Geophys. Res.- Atmos.*,

419 118, 2643-2655, <https://doi.org/10.1002/jgrd.50273>, 2013.

420 Kaufman, Y.J., Hobbs, P.V., Kirchhoff, V.W.J.H., Artaxo, P., Remer, L.A., Holben, B.N., King, M.D., Ward, D.E., Prins,

421 E.M., Longo, K.M., Mattos, L.F., Nobre, C.A., Spinhirne, J.D., Ji, Q., Thompson, A.M., Gleason, J.F., Christopher, S.A., and

422 Tsay, S.-C.: Smoke, clouds, and radiation-Brazil (SCAR-B) experiment, *J. Geophys. Res.-Atmos.*, 103, 31783-31808.

423 <https://doi.org/10.1029/98JD02281>, 1998.

424 Kolgotin, A., Müller, D., and Romanov, A.: Particle Microphysical Parameters and the Complex Refractive Index from

425  $3\beta+2\alpha$  HSRL/Raman Lidar Measurements: Conditions of Accurate Retrieval, Retrieval Uncertainties and Constraints to

426 Suppress the Uncertainties, *Atmosphere-Basel*, 14, 1159, <https://doi.org/10.3390/atmos14071159>, 2023.

427 Kulmala, M., Vehkamäki, H., Petaja, T., Maso, D. M., Lauri, A., Kerminen, V. M., Birmili, W., and McMurry, P.H.:

428 Formation and growth rates of ultrafine atmospheric particles: A review of observations, *J. Aerosol Sci.*, 35, 143-176,

429 <https://doi.org/10.1016/j.jaerosci.2003.10.003>, 2004.

430 Li, L., Li, C. C., Zhao, Y. M., Li, J., and Chu, Y. Q.: Geometrical constraint experimental determination of Raman lidar

431 overlap profile, *Appl. Optics*, 55, 4924-4928, <https://doi.org/10.1364/AO.55.004924>, 2016.

432 Lohmann, U., and Feichter, J.: Global indirect aerosol effects: a review, *Atmos. Chem. Phys.*, 5, 715-737,

433 <https://doi.org/10.5194/acp-5-715-2005>, 2005.

434 Martin, D. G., Apituley, A., and Donovan, P. D.: Feasibility study of integral property retrieval for tropospheric aerosol

435 from Raman lidar data using principle component analysis, *Appl. Optics*, 52, 2173-2186,

436 <https://doi.org/10.1364/AO.52.002173>, 2013.

437 Meskhidze, N., Sutherland, B., Ling, X., Dawson, K., Johnson, M. S., Henderson, B., Hostetler, C. A., Ferrare, R. A.:

438 Improving Estimates of PM<sub>2.5</sub> Concentration and Chemical Composition by Application of High Spectral Resolution Lidar

439 (HSRL) and Creating Aerosol Types from Chemistry (CATCH) Algorithm, *Atmos. Environ.*, 250, 118250,

440 <https://doi.org/10.1016/j.atmosenv.2021.118250>, 2021.

441 Miffre, A., Abou Chacra, M., Geffroy, S., Rairoux, P., Souhac, L., Perkins, R.J., and Frejafon, E.: Aerosol load study in

442 urban area by Lidar and numerical model, *Atmos. Environ.*, 44, 1152-1161, <https://doi.org/10.1016/j.atmosenv.2009.12.031>,

443 2010.

444 Moore, R. H., Wiggins, E. B., Ahern, A. T., Zimmerman, S., Montgomery, L., Campuzano Jost, P., Robinson, C. E.,

445 Ziemba, L. D., Winstead, E. L., Anderson, B. E., Brock, C. A., Brown, M. D., Chen, G., Crosbie, E. C., Guo, H., Jimenez, J.

446 L., Jordan, C. E., Lyu, M., Nault, B. A., Rothfuss, N. E., Sanchez, K. J., Schueneman, M., Shingler, T. J., Shook, M. A.,

447 Thornhill, K. L., Wagner, N. L., and Wang, J.: Sizing response of the Ultra-High Sensitivity Aerosol Spectrometer (UHSAS)

448 and Laser Aerosol Spectrometer (LAS) to changes in submicron aerosol composition and refractive index, *Atmos. Meas. Tech.*,

449 14, 4517-4542, <https://doi.org/10.5194/amt-14-4517-2021>, 2021.

450 Müller, D., Wandinger, U., and Ansmann, A.: Microphysical particle parameters from extinction and backscatter lidar

451 data by inversion with regularization: theory, *Appl. Optics*, 38, 2346-2357, <https://doi.org/10.1364/AO.38.002346>, 1999.

452 Müller, D., Hostetler, C. A., Ferrare, R. A., Burton, S. P., Chemyakin, E., Kolgotin, A., Hair, J. W., Cook, A. L., Harper,

453 D. B., Rogers, R. R., Hare, R. W., Cleckner, C. S., Obland, M. D., Tomlinson, J., Berg, L. K., and Schmid, B.: Airborne

454 Multiwavelength High Spectral Resolution Lidar (HSRL-2) observations during TCAP 2012: vertical profiles of optical and

455 microphysical properties of a smoke/urban haze plume over the northeastern coast of the US, *Atmos. Meas. Tech.*, 7, 3487-

456 3496, <https://doi.org/10.5194/amt-7-3487-2014>, 2014.



457 Siomos, N., Balis, D. S., Poupkou, A., Liora, N., Dimopoulos, S., Melas, D., Giannakaki, E., Filioglou, M., Basart, S.,  
458 and Chaikovskiy, A.: Investigating the quality of modeled aerosol profiles based on combined lidar and sunphotometer data,  
459 *Atmos. Chem. Phys.*, 17, 7003-7023, <https://doi.org/10.5194/acp-17-7003-2017>, 2017.

460 Veselovskii, I., Kolgotin, A., Griaznov, V., Müller, D., Wandinger, U., and Whiteman, D. N.: Inversion with  
461 regularization for the retrieval of tropospheric aerosol parameters from multiwavelength lidar sounding, *Appl. Optics*, 41,  
462 3685-3699, <https://doi.org/10.1364/AO.41.003685>, 2002.

463 Veselovskii, I., Kolgotin, A., Griaznov, V., Müller, D., Franke, K., and Whiteman, David. N.: Inversion of  
464 multiwavelength Raman lidar data for retrieval of bimodal aerosol size distribution, *Appl. Optics*, 43, 1180-1195,  
465 <https://doi.org/10.1364/AO.43.001180>, 2004.

466 Veselovskii, I., Whiteman, D. N., Kolgotin, A., Andrews, E., and Korenskii, M.: Demonstration of aerosol property  
467 profiling by multi-wavelength lidar under varying relative humidity conditions, *J. Atmos. Ocean. Tech.*, 26, 1543-1557,  
468 <https://doi.org/10.1175/2009JTECHA1254.1>, 2009.

469 Veselovskii, I., Dubovik, O., Kolgotin, A., Korenskiy, M., Whiteman, D. N., Allakhverdiev, K., and Huseyinoglu, F.:  
470 Linear estimation of particle bulk parameters from multi-wavelength lidar measurements, *Atmos. Meas. Tech.*, 5, 1135-1145,  
471 <https://doi.org/10.5194/amt-5-1135-2012>, 2012.

472 Vivekanandan, J., Ghate, V. P., Jensen, J. B., Ellis, S. M., and Schwartz, M. C.: A Technique for Estimating Liquid  
473 Droplet Diameter and Liquid Water Content in Stratocumulus Clouds Using Radar and Lidar Measurements, *J. Atmos. Ocean.  
474 Tech.*, 37, 2145-2161, <https://doi.org/10.1175/JTECH-D-19-0092.1>, 2020.

475 Wang, X. H., Di, H. G., Wang, Y. Y., Yin, Z. Z., Yuan, Y., Yang, T., Yan, Q., Li, S. C., Xin, W. H., and Hua, D. X.:  
476 Correction Method of Raman Lidar Overlap Factor Based on Aerosol Optical Parameters, *Acta Optica Sinica*, 43, 0601005,  
477 10.3788/AOS221295, 2023a.

478 Wang, X. H., Li, S. W., Hui, G. D., Li, Y., Wang, Y. Y., Yan, Q., Xin, W. H., Yuan, Y., and Hua, D. X.: Calibration  
479 method of Fernald inversion for aerosol backscattering coefficient profiles via multi-wavelength Raman-Mie lidar, *Opt.  
480 Commun.*, 528, 129030, <https://doi.org/10.1016/j.optcom.2022.129030>, 2023b.

481 Wang, N., Zhang, K., Shen, X., Wang, Y., Li, J., Li, C., Mao, J., Malinkad, A., Zhao, C., Russell, L., Guo, J., Gross, S.,  
482 Liu, C., Yang, J., Chen, F., Wu, L., Chen, S., Ke, J., Xiao, D., Zhou, Y., Fang, J., and Liu, D.: Dual-field-of-view high-spectral-  
483 resolution lidar: Simultaneous profiling of aerosol and water cloud to study aerosol–cloud interaction. *Proc. Natl. Acad. Sci.*,  
484 119(10): e2110756119, <http://doi.org/10.1073/pnas.2110756119>, 2022Wang, Z., and Sassen, K.: Cirrus Cloud Microphysical  
485 Property Retrieval Using Lidar and Radar Measurements. Part I: Algorithm Description and Comparison with In Situ Data.  
486 *Journal of applied Meteorology*. 41: 218-229. <https://doi.org/10.1175/1520-0469>, 2002.

487 Zhao, C. F., Qiu, Y. M., Dong, X. B., Wang, Z. E., Peng, Y. R., Li, B. D., Wu, Z. H., and Wang, Y.: Negative aerosol-  
488 cloud relationship from aircraft observations over Hebei, China, *Earth and Space Science*, 5, 19-29,  
489 <https://doi.org/10.1002/2017EA000346>, 2018.

490 Zhang, Y., Chen, S., Tan, W., Chen, S., Chen, H., Guo, P., Sun, Z., Hu, R., Xu, Q., Zhang, M., Hao, W., and Bu, Z.:  
491 Retrieval of Water Cloud Optical and Microphysical Properties from Combined Multiwavelength Lidar and Radar Data.  
492 *Remote Sens.* 13, 4396. <http://doi.org/10.3390/rs13214396>. 2021.